

SIMULATION OF FLOWS WITH PASSIVE POROSITY

Neal T. Frink, Steven X. S. Bauer, and Craig A. Hunter
NASA Langley Research Center
Hampton, Virginia, U.S.A.

Keywords: *unstructured, tetrahedral, Navier-Stokes, control, drag*

Abstract

A new passively porous boundary condition has been implemented into the USM3Dns, tetrahedral cell-centered, finite volume Euler and Navier-Stokes flow solver, and is applied for simulating control effectors on a generic General Aviation wing and an advanced fighter configuration, and for reducing drag on a ground transport vehicle. Each solution required a unique application of the porous boundary condition to the specific vehicle and flow condition. Existing data is used to calibrate the results for the general aviation wing and the ground vehicle with generally good agreement. The method is also used to investigate various configurations of porous control effectors on an advanced fighter configuration. Selected results from these three studies are summarized in the paper.

1 Introduction

Passive Porosity Technology (PassPorT) control effectors are one type of non-traditional or seamless control device that have been identified in systems studies conducted by NASA, DoD, and private industry. Because these devices are seamless, their first applications will be on military aircraft. However, because they weigh less, cost less to manufacture and maintain, and are less complex than traditional control effectors, they should readily be added to the suite of effectors used on commercial aircraft.

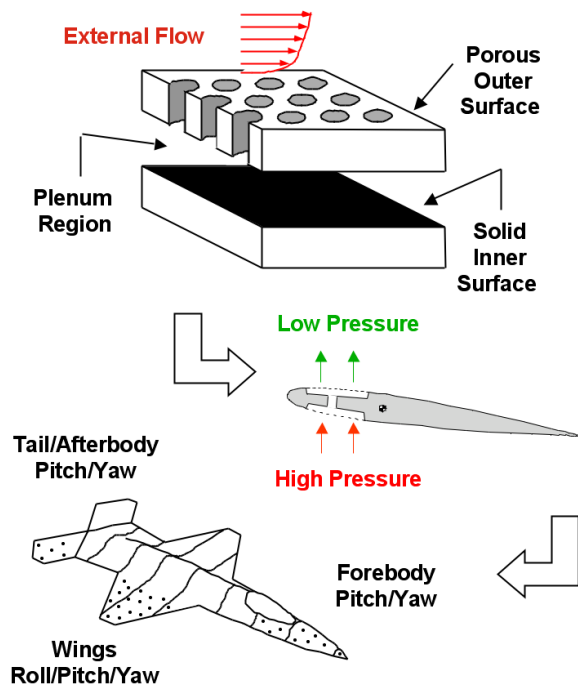


Fig. 1 The PassPorT concept and application as conformal control effector on military aircraft.

The underlying principle of PassPorT is illustrated in the upper sketch of Fig. 1 that depicts a porous skin positioned over a closed cavity/plenum region. Localized pressure differences due to flow over the outer surface of the wing “communicate” through the plenum in concert with small amounts of mass transfer in and out of the porous surface to alter its effective aerodynamic shape. For a properly designed system, the hole size is small with respect to the boundary layer thickness and is less than or equal to the skin thickness (an ideal hole diameter to skin thickness ratio should be 0.5 or less).

The aerodynamic integration of PassPorT control effectors will be a departure from current aircraft design methods. Typically, aircraft

airfoils are designed to maximize cruise performance, and then flaps (elevons, ailerons, etc.) are sized to provide sufficient moments to maintain control of the aircraft. With PassPorT effectors, the airfoils will be designed to generate a specified pressure distribution that can be modified by the actuation of the PassPorT device. This approach to aircraft design will require integration between structure and materials, aerodynamics, and guidance and control engineers.

Because PassPorT control effectors weigh and cost less than conventional effectors, the aircraft utilizing these effectors will have better performance at a lower price. Because PassPorT control effectors would be integrated into the wing across the span of the aircraft and because a large number of effectors would be distributed and controlled separately, the loss of one or several individual devices would not affect the controllability of the aircraft. This would provide an additional factor of safety to future aircraft.

PassPorT was originally applied to transonic airfoils to reduce the normal shock strength and thus, eliminate shock-induced separation and lower the drag levels [1-6]. With the success achieved in the wind-tunnel tests, a series of research efforts were conducted to develop Computational Fluid Dynamics (CFD) models to represent a passive porous system. The first studies utilized Darcy's Law [7]. These had limited success, but were fairly accurate as long as the coefficient required in the equation was chosen correctly. Later attempts with modified versions of Darcy's Law and utilizing some techniques used by researchers to determine oxygen transport through capillary walls were slightly more successful [8].

A more successful numerical model was devised in Ref. [9] to simulate normal flow through a screen positioned at a zonal-grid interface boundary. This model was derived to pass flow information across a common interface boundary separating an external

computational grid zone from an internal plenum grid zone. The screen characteristics are modeled on the interface by a contraction coefficient from Ref [9] that is determined from curve fits to experimental data following guidelines provided by Cornell [10] and Rouse [11]. A reformulation of this method as a surface boundary condition is presented in Ref. [12] to eliminate the need for constructing grid within an underlying plenum. This latter contribution greatly simplifies the numerical modeling of passively porous flow control systems and reduces computation cost.

The purpose of this paper is to review recent progress in applying numerical simulations of the PassPorT concept to aerodynamic problems. The simulations will be computed using the porous surface boundary condition of Ref. [12] and the USM3Dns tetrahedral unstructured flow solver [13]. Examples will be presented for using passive porosity as a control effector on a zero-sweep general aviation wing, and a tailless fighter aircraft concept. A novel application of PassPorT to reduce drag and enhanced fuel efficiency of tractor-trailer trucks will also be presented.

2. Computational Method

The numerical simulations are made using the NASA Tetrahedral Unstructured Software System (TetrUSS). The TetrUSS system [14] is comprised of loosely integrated, user-friendly software that enables the application of advanced Euler and Navier-Stokes tetrahedral finite volume technology to complex aerodynamic problems.

2.1 Grid Generation

The computational grids are constructed with the VGRIDns code that automatically generates tetrahedral unstructured grids suitable for computing Euler and Navier-Stokes flow solutions. The methodology is based on the

Advancing-Front method (AFM) [15] and the Advancing-Layers method (ALM) [16]. Both techniques are based on marching processes in which tetrahedral cells grow on an initial front (triangular boundary mesh) and gradually accumulate in the field around the subject geometry. VGRIDns is noted for its smooth high quality thin-layer viscous grids, and for a multidirectional anisotropic cell stretching capability. Work is also underway to develop a solution adaptive grid capability [17].

2.2 Flow Solver

USM3Dns [13] is a tetrahedral cell-centered, finite volume Euler and Navier-Stokes (N-S) flow solver. Inviscid flux quantities are computed across each cell face using Roe's [18] flux-difference splitting. Spatial discretization is accomplished by a novel reconstruction process [19], which is based on an analytical formulation for computing solution gradients within tetrahedral cells. The solution is advanced to a steady state condition by an implicit backward-Euler time-stepping scheme [20]. Flow turbulence effects are modeled by the Spalart-Allmaras (S-A) one-equation model [21], that is optionally coupled with a wall function to reduce the number of cells in the sublayer region of the boundary layer.

USM3Dns runs on massively parallel personal computer (PC) clusters and Origin 2000 machines [22], and on Cray vector processors with multitasking. Memory is allocated dynamically. The code requires 175 eight-bit words per tetrahedra, and runs with individual processor times of 230 μ sec/cell/cycle on a single CPU of an Origin 2000, and 34 μ sec/cell/cycle on a Cray-C90.

2.3 Porous surface boundary conditions

The porous surface boundary condition in Ref. [12] was developed through a collaborative effort among an experimental porosity expert

and code experts for two structured-grid flow solvers, TLNS3D [23,24] and CFL3D [25], and one unstructured solver, USM3Dns [13]. The new boundary condition is an extension of the theory developed by Bush [9] to model flow through a screen. Bush's original model was derived to pass flow information across a pseudo interface boundary separating an external flow and an internal plenum. In the revised approach, the Bush model was re-formulated as a surface boundary condition for the external, thus eliminating the need to grid and compute flow within the plenum side of a porous surface.

Conservation laws from steady, one-dimensional (1D), isentropic, and adiabatic gas dynamics are used to model flow through the porous surface, in conjunction with the assumption of a constant plenum pressure and the requirement of zero net mass flow through the porous surface. Part of the solution procedure involves a feedback iteration to update the plenum pressure and drive net mass flow to zero. Because of the 1D equations used in the boundary condition, only the surface porosity level is specified, not the actual porous hole geometry (circular holes of 0.020-0.050 inch diameter are typically used in wind tunnel and flight applications of passive porosity). Based on previous aerodynamic testing [26], a porosity level of 22% openness was used in the following studies.

3 Selected Applications

Results will be highlighted for the application of passive porosity as a control effector on a zero-sweep general aviation wing, and a tailless fighter aircraft concept. A novel application of PassPorT to reduce drag and enhance fuel efficiency of tractor-trailer trucks will also be presented. While most of the following computational solutions are generated from USM3Dns, some supporting solutions from TLNS3D and CFL3D are included.

3.1 Effectors

3.1.1 GA(W)-1 Wing

The GA(W)-1 [General Aviation (Whitcomb) – 1] wing [27] was investigated both experimentally and computationally to measure the effectiveness of leading-edge porosity for generating lateral-directional control power. The wing semispan surface definition, depicted in Fig. 2, consists of a rectangular planform wing of aspect ratio 3 with 0° leading-edge sweep. Porosity was applied to the shaded leading-edge region ahead of the 18-percent chord station.

The computational assessment published in Ref. [12] compared the implementation of the porous surface boundary condition into one unstructured and two structured flow solvers. An unstructured tetrahedral grid of 1,681,831 cells was constructed for the USM3Dns code, whereas a structured hexahedral grid with $193 \times 65 \times 33$ hexahedral cells was generated for the structured multiblock codes TLNS3D and CFL3D. Farfield boundaries were placed 10 chord lengths away from the wing in all directions on which a characteristic inflow/outflow boundary condition was applied. The no-slip condition was applied to the wing solid surfaces, with the exception that USM3Dns utilized a wall function. When

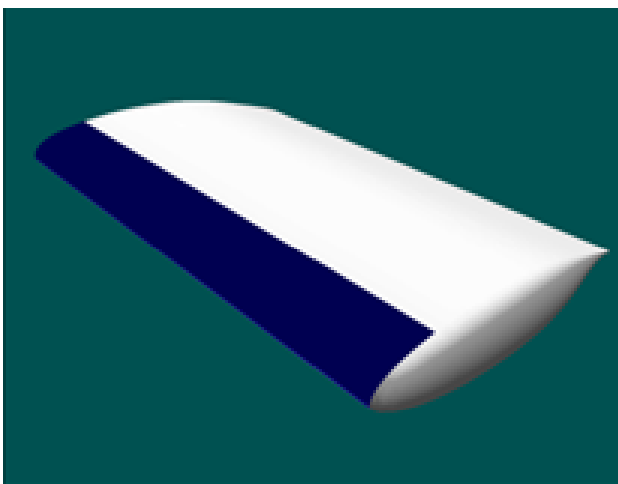


Fig. 2 Semispan surface geometry for GA(W)-1 wing. Porosity applied to shaded region around leading edge.

applying leading-edge porosity, a 22-percent openness condition was prescribed to the darkened region denoted in Fig. 2.

Navier-Stokes flow solutions were computed at $M_\infty=0.17$, $\alpha=0$ and 8 degrees, and a chord Reynolds number of 3.5 million. The plenum pressure was determined from USM3Dns and provided as input for the other codes. The nondimensional values of plenum pressure used for $\alpha=0$ and 8 degrees were 0.7130 and 0.7156, respectively, where freestream pressure is 0.7143.

Figure 3 compares the chordwise C_p distributions at $\alpha=8$ deg. and $2y/b=0.67$ (one chord length from the symmetry plane) between the code results and experimental data for the solid and porous surfaces. The experimental data reveals a dramatic loss of leading-edge suction peak and consequent loss of lift due to passive porosity. The solid surface computational results are nearly identical between the codes and are in generally good agreement with the experimental data, with the exception of the leading-edge suction peak. The porous leading-

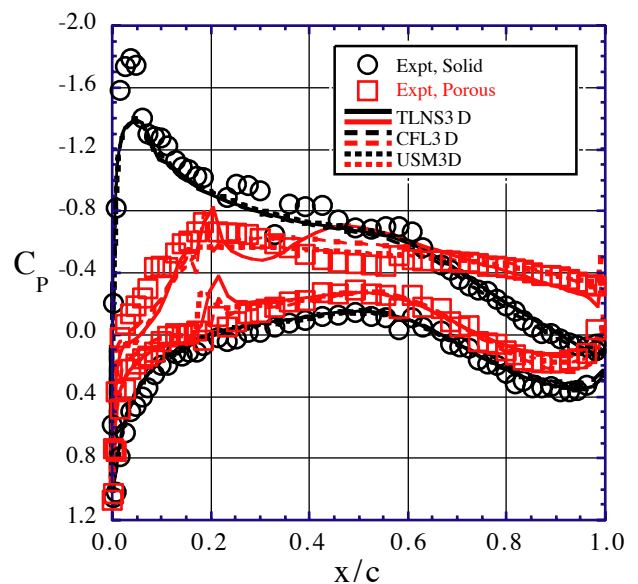


Fig. 3 C_p comparison of solid and porous GA(W)-1 wing for TLNS3D, CFL3D, and USM3Dns with experiment $2y/b=0.67$, $M_\infty=0.17$, $\alpha=8$ deg., and $Re_c=3.5$ million.

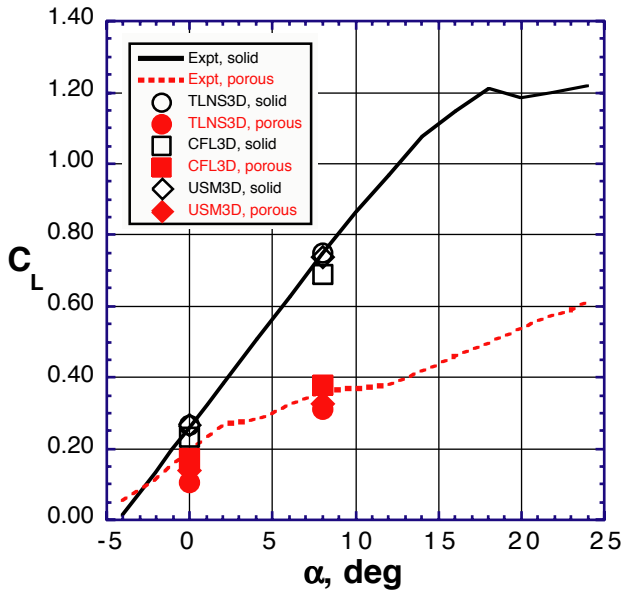


Fig. 4 Comparison of lift characteristics of solid and porous leading edge for GA(W)-1 wing. $M_\infty=0.17$ and $Re_c = 3.5$ million.

edge computations show some variation between codes, but are in reasonably good agreement with the data.

Figures 4 and 5 illustrate the large impact of leading-edge porosity on lift and drag coefficients, and demonstrate that the porosity boundary condition model yields correct estimates of those effects at angles of attack of 0 and 8 degrees. With leading-edge porosity having such a large effect on lift and drag, an asymmetric application of this device could be envisioned for lateral-directional control in place of moving control surfaces. The relatively good agreement of the numerical results with experimental data suggest that the porous boundary condition model could serve as a useful supplemental design tool in what was previously an experimentally intensive process.

3.1.2 ACWFT configuration

The goal of this work was to develop a passive porosity control effector system for a tailless fighter aircraft concept. Results discussed here will summarize longitudinal (pitch) maneuver control at low-speed, high angle of attack conditions. The aircraft used in this investigation is based on fighter configurations

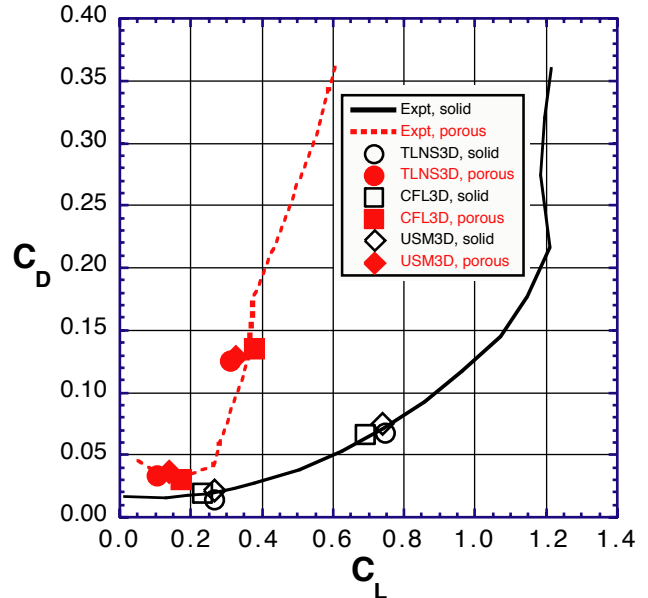


Fig. 5 Comparison of drag characteristics of solid and porous leading edge for GA(W)-1 wing. $M_\infty=0.17$ and $Re_c=3.5$ million.

developed under the Air Force Wright Lab “Aero Configuration/Weapons Fighter Technology” (ACWFT) program [28]. The aim of this program was to develop multi-mission fighter aircraft configurations with advanced technologies and performance characteristics capable of addressing post-year-2000 needs and threats. For passive porosity design work, a simplified aircraft configuration was developed by extracting salient features of the ACWFT “1204” configuration.

USM3Dns results for the simplified ACWFT 1204 configuration at $M_\infty = 0.14$ and $\alpha = 28^\circ$ are given in Figure 6, where pressure coefficient (C_p) contours and particle traces over the upper surface of the aircraft are shown. These results are typical for a chined body at high angle of attack. Two large vortices track along the upper surface of the forebody (red and green traces), and wing flow is characterized by a spanwise vortex originating from each leading-edge wing-body junction (blue traces). These vortical flows create significant low-pressure regions along the aircraft’s upper surface, with a typical C_p level of about -2 .

Five passive porosity configurations were developed to effect nose-down pitch control, and are shown in Figure 7. Configurations P1

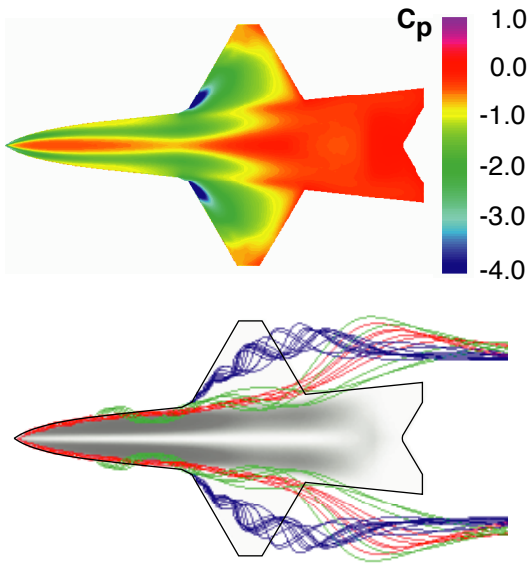


Fig. 6 Upper Surface Pressure Coefficient and Particle Traces from USM3Dns – Baseline Configuration ($M = 0.14$, $\alpha = 28^\circ$).

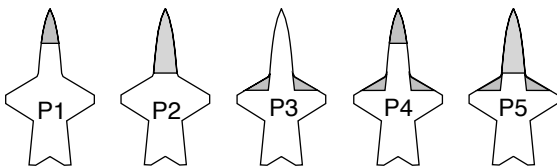


Fig. 7 Passive Porosity Nose-down Pitch Control Effector Configurations. Shaded regions indicate upper and lower surface porosity.

and P2 apply porosity to the forebody region (FB), starting at the nose and going back to $FS = 147$ (covering 33% of the forebody surface area) and $FS = 298$ (covering 100%), respectively. Configuration P3 applies porosity to the leading-edge wing-body junction region, forward of the aircraft CG at $FS = 365$. Configurations P4 and P5 are combinations of the P1, P2, and P3 designs. Configurations P1 and P3 will be discussed in some detail; the others summarized.

Results for the P1 configuration are shown in Figure 8, where surface C_p is plotted versus polar angle around the forebody at $FS = 100$, along with the baseline configuration. It is obvious that the application of passive porosity

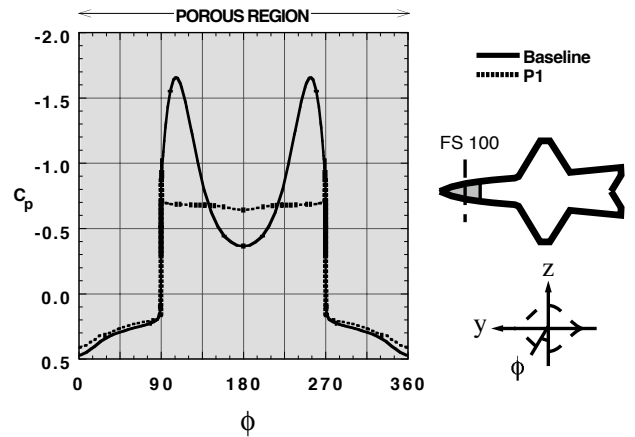


Fig. 8 Comparison of Forebody Surface Pressure Coefficient at $FS = 100$ from USM3Dns. Baseline and P1 Pitch Control Configuration.

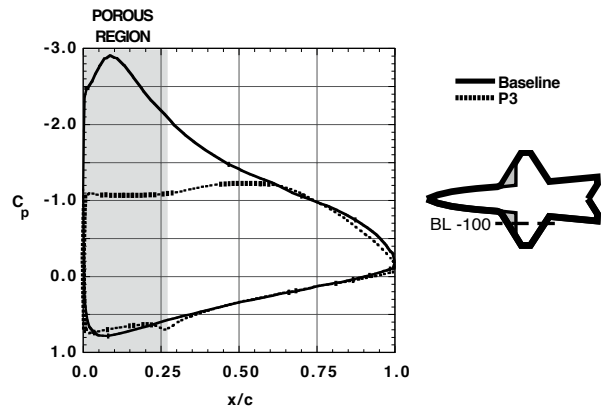


Fig. 9 Comparison of Wing Surface Pressure Coefficient at $BL = -100$. Baseline and P3 Pitch Control Configuration.

resulted in a large overall increase in local pressure on the forward upper surface of the forebody, but pressure on the lower surface was virtually unchanged (as would be expected). At the $FS = 100$ location, the upper surface pressure in the P1 configuration is nearly constant at $C_p \approx -0.65$, leveling out the suction peaks of the baseline configuration.

A C_p plot for the P3 configuration (taken at the spanwise location $BL = -100$) is given in Fig. 9. These results show that the application of passive porosity increased pressure and smoothed out pressure gradients the leading-edge wing-body junction region. The wing's suction peak was leveled off to a near constant

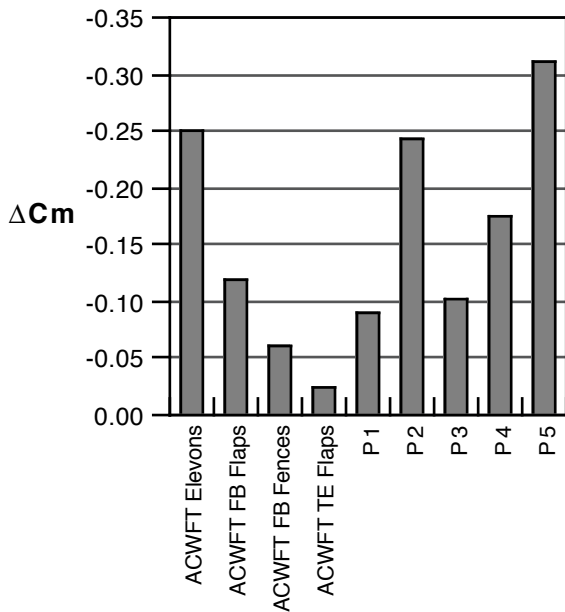


Fig. 10 Nose-down Pitch Control Summary

value over much of the upper surface, while the lower surface pressure was largely unaffected.

Nose-down pitch control effectiveness for the five passive porosity configurations in Fig. 7 is summarized in Fig. 10 relative to data for selected ACWFT pitch control effectors [28]. The passive porosity control effectors provided nose-down pitch increments ranging from $\Delta C_m = -0.089$ for the P1 configuration to $\Delta C_m = -0.31$ for the P5 configuration, comparing favorably to the range of ACWFT devices and conventional controls. Both the P2 and P5 configurations provided enough nose-down pitch increment to reach “absolute” nose-down control ($\Delta C_m = -0.24$), countering the configuration’s inherent nose-up pitching moment at the $M_\infty = 0.14$, $\alpha = 28^\circ$ condition. With increments of $\Delta C_m = -0.243$ and $\Delta C_m = -0.31$, respectively, the P2 and P5 configurations roughly equaled or exceeded the $\Delta C_m = -0.25$ provided by the conventional ACWFT elevons deflected to 60° .

3.2 Drag control on tractor-trailer ground vehicles

There are nearly 2 million tractor-trailer rigs on the road in the United States that travel a

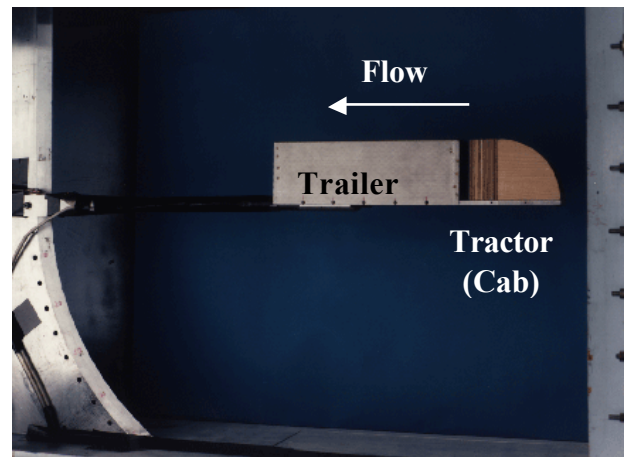


Fig. 11 Porous Truck Model in the NASA LaRC Subsonic Basic Research Tunnel (SBRT)

cumulative 120 billion miles/year (193 billion kilometers/year). The average fuel economy is about 6 miles/gallon (2.55 kilometers/liter) that translates into 20 billion gallons/year (76 billion liters/year). Thus, even relatively small reductions in drag can lead to very large savings in the yearly U.S. fuel consumption and pollution. Many studies have been conducted on drag reduction of tractor-trailer rigs. However, most efforts have concentrated on improving the tractor aerodynamics, while very little attention has been focused on the trailer.

A wind-tunnel test was conducted in the NASA Langley Research Center (LaRC) Subsonic Basic Research Tunnel (SBRT) on a simulated tractor-trailer geometry (Fig. 11). Three tractor cab shapes were tested, rectangular, wedge-shaped, and rounded (quarter circle), as well as several tractor-trailer gap spacing configurations. The documented results by Sovran et. al. [29] were verified during the initial phase of this experimental study.

The rounded cab configuration was chosen for the numerical simulation study with the gap filled between the base of the cab and the trailer. The trailer was constructed with 30% porosity over the entire surface. Covering the interior side of the holes with adhesive tape simulated a solid surface. Porous surface regions were prescribed by simply leaving the appropriate inside surface untaped. Data from the wind-

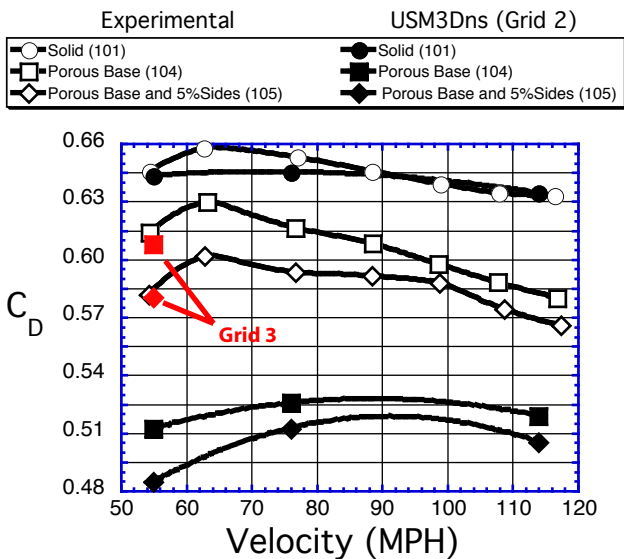


Fig. 12 Experimental and USM3Dns Drag Coefficient Values for the Solid (101), Porous Base (104), and Porous Base with 5% on the sides and top upstream of the base (105).

tunnel test were taken over a range of Mach numbers from 0.025 to 0.154 (19 to 117 miles/hour, or 31 to 188 kilometers/hour), but only the data from 55 miles/hour (88.5 kilometers/hour) to 117 miles/hour will be discussed in the following.

The drag data acquired during the test is plotted in Fig. 12 (as open symbols) for three configurations. The baseline configuration (101) was a solid box (all the surfaces taped from within). The second configuration (104) had a porous base. The third configuration (105) had a porous base plus an additional inch of porous surface on the sides and top just upstream of the base (equivalent to 5% of the length). Configuration 104 had a reduction in drag of approximately 5% to 8% (increasing with increasing velocity). Configuration 105 maintained a 10% to 11% reduction in drag over the baseline for the velocity range measured.

Also shown in the Fig. 12 are results from a numerical simulation investigation utilizing USM3Dns with the porous surface boundary condition. Three grids of increasing density were generated to establish the necessary clustering to achieve a meaningful result. The first (Grid 1) had 650,000 tetrahedral cells, did not adequately resolve the base region of the vehicle to capture the wake, and is not shown.

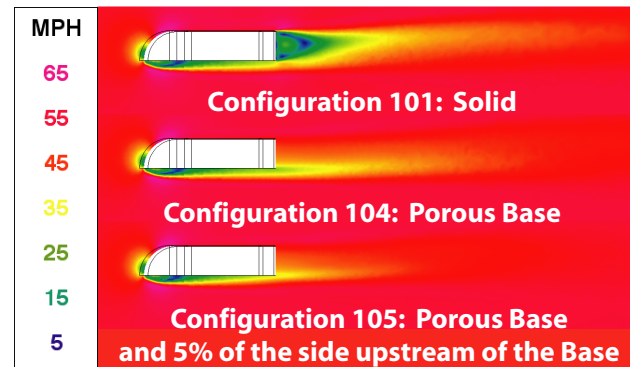


Fig. 13 USM3Dns velocity contours with Grid 3 for the Solid (101), Porous Base (104), and Porous Base with 5% on the sides and top upstream of the base (105).

The second (Grid 2) having 3 million tetrahedra resolved the physics in the wake region much better and eventually converged for the solid solution. However for this grid, the computed drag coefficients from the porous base solutions (solid symbols) were significantly lower than their experimental counterparts. The lower predicted drag from the numerical simulation is primarily caused by the porous boundary condition driving the base pressure to near the freestream value.

The third (Grid 3: illustrated by the red solid symbols in Fig. 12) had 4.5 million tetrahedra and also utilized a lower level of porosity in the boundary condition routine (nearly reaching the practical upper limit of 98% solidity). The solid solution produced the same results as the Grid 2, but the two porous solutions predicted more base drag and came very close to matching those seen in the wind-tunnel (recall that the Grid 2 had nearly zero base drag because the base pressure had returned close to freestream conditions). However, the solution did not converge as well as the other volume grids utilizing solidity levels of 78% even though the solutions ran for over 2000 iterations.

Figure 13 illustrates the reduction in wake size due to base porosity using shaded speed contours. The solid base solution at the top has a well-defined circulation region in the wake, whereas both porous configurations have



Baseline (Configuration 101) vehicle on wet road
(right lane)



Porous (Configuration 105) vehicle on wet road
(right lane)

Fig. 14 Comparison of water vapor spray behind a baseline and a passive porous trailer.

essentially no wake associated with the blunt base. Figure 14 shows actual tractor-trailer rigs operating on a wet highway. The top photo shows the baseline (configuration 101) vehicle with a solid trailer (right lane). Note, the spray from the wet road fills the base of the vehicle much as is indicated in the computational solution in Fig. 13. The lower photo shows the configuration 105 vehicle (right lane). An absence of spray is observed in the wake behind the vehicle indicating no wake recirculation region to suction the water vapor up into the void in the wake/base flow region. Note, the same truck passing to the left of the test vehicle

in both cases gives an additional reference point on the extent of water vapor behind a solid base.

The numerical simulations have provided valuable insight into how the porous surfaces reduce the recirculation in the base wake flow behind a tractor trailer. While the predicted drag reduction was significantly larger for the converged porous solutions, the trends with increasing velocity were well represented. Furthermore, evidence of the reduction in recirculating flow behind the trailer is consistent between the numerical simulation visualization and the spray photographs taken behind a road-test vehicle. These results as well as those acquired during the road test of the concept have led to a NASA patent [30]. The ground transportation fleets should hopefully utilize this new drag reduction technology in the future.

4. Concluding Remarks

Recent progress in applying numerical simulations of the PassPorT concept to aerodynamic problems has been presented. The simulations were computed using a new porous surface boundary condition that has been installed in the USM3Dns tetrahedral unstructured flow solver, and in two structured-grid flow solvers, TLNS3D and CFL3D.

Two examples were presented for using passive porosity as a control effector on a zero-sweep general aviation wing, and a tailless fighter aircraft concept. In both cases, significant and ample control power was demonstrated for both longitudinal and lateral-directional control with no external moving surfaces.

A novel application of PassPorT to reduce drag and enhance fuel efficiency of tractor-trailer trucks was also presented. Numerical simulations with the porous boundary condition confirmed both experimentally measured drag reduction and visual evidence of reduced wake recirculation behind a road-test vehicle. If applied to the entire tractor-trailer fleet in the

U.S., this technology could potentially save over \$1 billion per year in fuel costs.

For each of these examples, the relatively good agreement of the numerical results with experimental data suggest that the new porous boundary condition model could serve as a useful supplemental design tool in what was previously an experimentally intensive process.

References

1. Thiede P, Krogmann P and Stanewsky E. Active and passive shock/boundary layer interaction control on supercritical airfoils. AGARD-CP-365, May 1984.
2. Bahi L and Ross J. Passive shock wave/boundary layer control for transonic airfoil drag reduction. AIAA Paper 83-0137, January, 1983.
3. Nagamatsu H, Brower W Jr, Bahi L and Marble S. Investigation of passive shock wave/boundary layer control for transonic airfoil drag reduction. Rensselaer Polytechnic Institute, Troy, NY, First Annual Report for NASA Grant No. NSG 1624, October 1, 1979 to September 30, 1980.
4. Savu G, Trifu O and Dumitrescu L. Suppression of shocks on transonic airfoils. *Proceedings of the International Symposium on Shock Tubes and Waves*. Sydney, August 19-22, 1983.
5. Savu G and Trifu O. Porous airfoils in transonic flow. *AIAA Journal*, Vol. 22, No. 7, July 1984, pp 989-991.
6. Nagamatsu H and Orozco R. Porosity effect on supercritical airfoil drag reduction by shock wave/boundary layer control. AIAA-84-1682, June 1984.
7. Hartwich P. Euler study on porous transonic airfoils with a view toward multipoint design. *Journal of Aircraft*, Vol. 30, No. 2, pp. 184-191, 1993.
8. Kraushaar S and Chokani N. Improved models for the porous surface with passive control. Masters Thesis North Carolina State University, 1996.
9. Bush R. Engine face and screen loss models for CFD applications. AIAA Paper 97-2076, June 1997.
10. Cornell W. Losses in flow normal to plane screens. *Transactions of the ASME*, pp 791-799, May 1958.
11. Rouse H. *Elementary Mechanics of Fluids*. Dover Publications, 1978 (originally published John Wiley and Sons, Inc., 1946), p 57.
12. Frink N, Bonhaus D, Vatsa V, Bauer S and Tinetti A. A boundary condition for simulation of flow over porous surfaces. AIAA Paper 2001-2412, June 2001.
13. Frink N. Tetrahedral unstructured Navier-Stokes method for turbulent flows. *AIAA Journal*, Vol. 36, No. 11, pp 1975-1982, 1998.
14. Frink N, Pirzadeh S, Parikh P, Pandya M and Bhat M. The NASA tetrahedral unstructured software system (TetrUSS). *The Aeronautical Journal*, Vol. 104, No. 1040, pp 491-499, 2000.
15. Löhner R and Parikh P. Three-dimensional grid generation by the advancing front method. *Int.J.Num.Meth. Fluids* 8, pp 1135-1149 (1988).
16. Pirzadeh S. Three-dimensional unstructured viscous grids by the advancing layers method. *AIAA Journal*, Vol. 34, No. 1, pp. 43-49, 1996.
17. Pirzadeh S. A solution adaptive technique using tetrahedral unstructured grids. ICAS2000-2.6.2, presented at the 22nd International Congress of Aeronautical Sciences, Harrogate United Kingdom, Aug. 27-Sept. 1, 2000.
18. Roe P. Characteristic based schemes for the Euler equations. *Annual Review of Fluid Mechanics*, Vol. 18, pp 337-365, 1986.
19. Frink, N. Recent progress toward a three-dimensional unstructured Navier-Stokes flow solver. AIAA 94-0061, January 1994.
20. Anderson W and Bonhaus D. An implicit upwind algorithm for computing turbulent flows on unstructured grids. *Computers Fluids*, Vol. 23, No. 1, pp 1-21, 1994.
21. Spalart P and Allmaras S. A one-equation turbulence model for aerodynamic flows. AIAA Paper 92-0439, January 1992.
22. Bhat M and Parikh P. Parallel implementation of an unstructured grid-based Navier-Stokes solver. AIAA 99-0663, January 1999.
23. Vatsa V and Wedan B. Development of a multigrid code for 3-D Navier-Stokes equations and its application to a grid-refinement study. *Computers and Fluids*, Vol. 18, No. 4, pp 391-403, 1990.
24. Vatsa V, Sanetrik M and Parlette E. Development of a flexible and efficient multigrid-based multiblock flow solver. AIAA Paper No. 93-0677, Jan. 1993
25. Krist S, Biedron R and Rumsey C. *CFL3D user's manual*. November 1996.
26. Bauer S and Hernandez G. Reduction of cross-flow shock-induced separation with a porous cavity at supersonic speeds. AIAA Paper 88-2567, June 1988.
27. McGhee R and Beasley W. Low-speed aerodynamic characteristics of a 17-percent-thick airfoil section designed for general aviation applications. NASA TN D-7428. December 1973
28. Hunter C, Viken S, Wood R and Bauer S. Advanced aerodynamic design of passive porosity control effectors. AIAA Paper 2001-0249, January 2001.
29. Sovran G; Morel T and Mason W Jr. Aerodynamic drag mechanisms of bluff bodies and road vehicles. General Motors Research Laboratories, Plenum Press, New York, 1978.
30. Bauer S and Wood R. Base passive porosity for drag reduction. *United States Patent Number 6,286,892*, September 11, 2001.